

# Ulysses spacecraft observations of radio and plasma waves: 1991-1995

R.J. MacDowall<sup>1</sup>, R.A. Hess<sup>2</sup>, N. Lin<sup>3</sup>, G. Thejappa<sup>4</sup>, A. Balogh<sup>5</sup>, and J.L. Phillips<sup>6</sup>

<sup>1</sup> NASA, Goddard Space Flight Center, Code 695, Greenbelt, Maryland, 20771, USA

<sup>2</sup> Hughes STX Corporation, Lanham, Maryland, 20706, USA

<sup>3</sup> School of Physics and Astronomy, University of Minnesota, Minneapolis, Minnesota, 55455, USA

<sup>4</sup> Department of Astronomy, University of Maryland, College Park, Maryland, 20740, USA

<sup>5</sup> The Blackett Laboratory, Imperial College, London SW7 2BZ, UK

<sup>6</sup> Los Alamos National Laboratory, MS D466, Los Alamos, New Mexico, 87545, USA

Received 22 March 1996 / Accepted 16 July 1996

**Abstract.** The radio and plasma wave investigation of the Ulysses spacecraft mission provided nearly continuous observations of wave electric fields (less than 1 MHz) and magnetic fields (less than 450 Hz) from spacecraft launch in late 1990 through perihelion in 1995 and beyond. The Ulysses spacecraft reached heliographic latitudes of  $\pm 80^\circ$ , providing a unique opportunity to study wave activity in fast solar wind emanating from polar coronal holes and to examine the differences relative to waves in the streamer belt. These data led to the discovery that many magnetic field depressions (magnetic holes) are populated by waves at the electron plasma frequency; such phenomena occur much more frequently in high-latitude, fast solar wind. At high latitudes, Ulysses frequently detected the waves conventionally assumed to be ion-acoustic waves; however, the electron-proton temperature ratio at these latitudes is always less than one, suggesting that the waves must be some other mode. Electrostatic and electromagnetic waves at lower frequencies also evidenced marked changes as Ulysses recurrently entered and exited the streamer belt during the “fast latitude scan” phase of its orbit. These variations with heliographic latitude, as well as variations with distance from the Sun, are presented and interpreted.

**Key words:** plasmas – waves – solar wind – interplanetary medium

---

## 1. Introduction

Prior to the Ulysses spacecraft mission, the in situ exploration of the inner heliosphere was limited to heliographic latitudes within  $\sim 20^\circ$  of the equatorial plane. The regions of fast solar wind emanating from solar coronal holes could only be explored

when they descended near the heliographic equator. Ulysses is the first spacecraft to provide direct access to high heliographic latitudes, as shown in Fig. 1. A particularly interesting feature of the trajectory is the “fast latitude scan”, taking the spacecraft from  $-80^\circ$  to  $+80^\circ$  in less than 10 months. This rapid South-to-North pass through the interplanetary medium (IPM) provides observations that are nearly independent of radial distance and evolution of the solar cycle. The orbit also provides access to long intervals when the spacecraft is continuously in fast wind and when the Sun-spacecraft distance changes significantly with only limited changes in latitude.

The Unified Radio and Plasma Wave Investigation (URAP) has provided nearly continuous electric field observations from DC to 940 kHz and magnetic field observations from 0.22 to 450 Hz (Stone et al. 1992) throughout the Ulysses mission. These observations extend the exploration of the solar wind plasma wave environment initiated by wave instruments on the Helios, Voyager, ISEE, and other spacecraft. Waves observed in the frequency ranges of such instruments are typically divided into the three classes shown in Table 1 (Gurnett 1991), although it is recognized that there are a variety of problems with this classification. The details of the generation mechanisms and the source locations are not certain. For example, the wave activity occurring at the electron plasma frequency  $f_{pe}$  is presumed to be Langmuir mode; however, the source location of many of these waves has only recently been identified to be magnetic holes (Lin et al. 1995). The electrostatic waves frequently detected in the frequency range between  $f_{pe}$  and the ion plasma frequency  $f_{pi}$  are often identified as Doppler-shifted ion-acoustic waves (Gurnett 1991, and references therein). However, ion-acoustic waves are strongly damped when  $T_e/T_i < 3-5$ , and the waves referred to as ion-acoustic-like waves are frequently detected during such intervals (Hess et al. 1996; Thejappa et al. 1996). The source of electromagnetic waves less than the electron cyclotron frequency  $f_{ce}$ , which may play a role in heat-flux regulation, is not well understood (Gary et al. 1994; Thejappa et

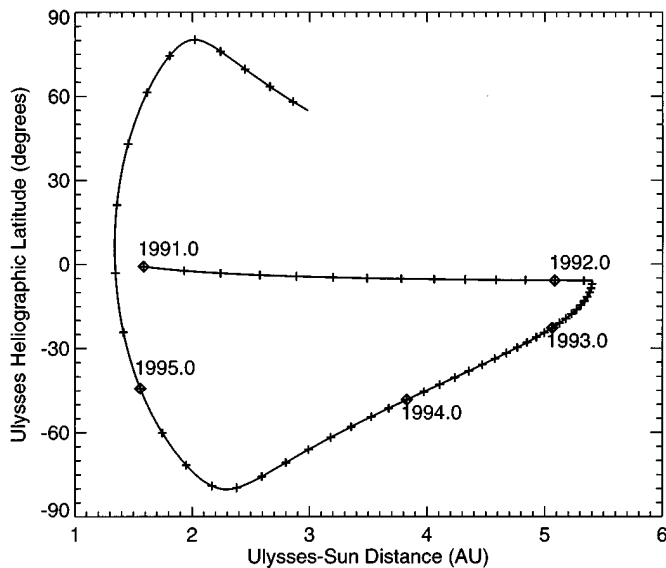


**Fig. 1.** Position of Ulysses as a function of distance from the Sun (AU) and heliographic latitude (degrees). Tick marks indicate the start of each month from 1991–1995; diamonds indicate the start of the year.

al. 1995). Indeed, there remain numerous questions about the sources and consequences of most of the plasma modes occurring in the solar wind.

The Ulysses URAP observations can be used to provide new constraints on the sources and evolution of plasma wave activity. In this paper, an overview of the observations from three of the URAP instruments is provided for the period 1991 through 1995. These observations convey the marked differences between the wave environment in slow and fast solar wind, as observed around the time of solar minimum. A key goal of the paper is to present the data in a manner that permits visualization of the time variability of the wave activity in different frequency regimes. The paper also examines the variations in wave activity as a function of distance from the Sun and discusses some of the consequences for particle transport, electron heating, and solar wind heat flux regulation in the solar wind. Even after more than 20 years of exploring solar wind plasma wave phenomena, there are new discoveries to be made.

## 2. Instrumentation and datasets

The observed character of sampled wave activity depends on the capabilities of the instrument; therefore, appropriate information is included here to permit interpretation of the URAP data. In this paper, we describe the wave measurements obtained by the Radio Astronomy Receiver (RAR), Plasma Frequency Receiver (PFR), and Waveform Analyzer (WFA), which comprise three of the six instruments making up the URAP investigation. A more complete description of each of the instruments can be found in Stone et al. (1992). The RAR consists of four super-heterodyne radio receivers, which cover two bands (1.25 to 48.5 kHz and 52 to 940 kHz) and can be connected to three electric field antenna configurations. Specifically, two of the receivers

are connected to the spin-axis monopole and two receivers are connected to either the spin-plane dipole antenna or to the summation of signals from the spin-plane and spin-axis antennas. The summation configuration is used to facilitate determining the direction to a remote radio source (Manning and Fainberg 1980). The spin plane antenna consists of a pair of wire booms, each 35 m long, which form a dipole of 72 m tip-to-tip length. The spin-axis monopole is a 7.5 m boom, whose effective electrical length is less than 4 m. The PFR receivers cover the range from 0.57 to 35 kHz with continuous, logarithmically-spaced frequency steps, large dynamic range, and good time resolution. One of the two PFR receivers is connected to the spin-plane dipole; this combination provides the data presented in this paper. The WFA provides spectral analysis in the range from 0.08 to 448 Hz for both electric and magnetic fields. In this paper, only data from the spin-plane electric field antenna and the spin plane search coil are presented. Table 2 lists the frequency ranges, bandwidths, numbers of channels, typical time resolutions, and threshold levels of the receiver/antenna combinations for which data are presented.

The time resolution of the data presented here is either 1 hour or 10 minutes, as indicated in the figure captions. For all instruments, except the PFR, the data are averaged over the relevant time interval. For the PFR, the data are the peak values detected during the indicated time interval. The URAP data presented here are derived from data products that are archived at the National Space Science Data Center (NSSDC) and, consequently, available to the space physics community.

Solar wind data from the Ulysses plasma instrument (Bame et al. 1992) and Ulysses magnetic field data (Balogh et al. 1992) are used to identify correlations between variations in wave intensities and solar wind parameters, such as solar wind speed, electron density, electron and ion temperatures, and magnetic field magnitude. The plasma measurements for electrons cover the energy range 0.86 eV to 814 eV; ions are detected between 255 eV/q and 34.4 keV/q. The plasma data presented here are hour average data. The magnetic field instrument consists of a flux-gate and a vector helium magnetometer for redundancy and cross-calibration; the data presented here are 10 minute averages.

## 3. Observations

### 3.1. Wave activity along the Ulysses trajectory

Fig. 2 provides a synopsis of several of the varieties of wave activity observed by URAP through 1995; the data have 1 hour resolution. Single frequency plots are used to provide the best time and intensity resolution; the scatter observed in the data provides an indication of the burstiness of the wave activity. Dynamic spectra plots published elsewhere (Stone et al. 1995, Hoang et al. 1996) provide a better indication of the frequency-dependent behavior of these emissions.

The five panels in Fig. 2 present data from five different combinations of URAP antennas and receivers. Panels (a and b) present 940 and 42 kHz electric field data, respectively, from the

**Table 1.** Wave mode classification

Frequency	Likely modes	Likely instabilities	Selected references
$f \sim f_{pe}$	Langmuir waves	electron beams	Bohm and Gross (1949) Scarf et al. (1971) Filbert and Kellogg (1979) Lin et al. (1986) Kellogg et al. (1992) Thejappa et al. (1993)
$f_{pi} < f < f_{pe}$	Doppler-shifted ion-acoustic waves	electron heat flux, ion-beam instability	Gurnett and Frank (1978) Rodriguez (1981) Gary (1993)
	electron acoustic waves	electron-beam instability	Thompsen et al. (1983) Marsch (1985) Gary (1993)
$f < f_{ce}$	whistler waves	Doppler-shifted cyclotron resonance, electron heat flux, currents	Coroniti et al. (1982) Vaisberg et al. (1983) Tokar et al. (1984)
	lower hybrid waves		Marsch and Chang (1983) Gary (1993) Thejappa et al. (1995)

**Table 2.** Ulysses URAP instrument parameters (for data in this paper)

Name	Antenna	Frequency Range	Bandwidth	Channels	Typical Time Resolution	Typical Background Level
Radio Astronomy Receiver (high band)	usually spin-plane dipole + spin-axis monopole	52–940 kHz	3 kHz	12	144 sec	$2 \cdot 10^{-8} \text{ V Hz}^{-1/2}$ @ 940 kHz
Radio Astronomy Receiver (low band)	usually spin-plane dipole	1.25–48.5 kHz	0.75 kHz	64	128 sec	$1 \cdot 10^{-8} \text{ V Hz}^{-1/2}$ @ 42 kHz
Plasma Frequency Receiver	spin-plane dipole	0.57–35 kHz	14% of center frequency	32	16 sec	$1 \cdot 10^{-6} \text{ V Hz}^{-1/2}$ @ 3 kHz
Waveform Analyzer E-field	spin-plane dipole	0.08–448 Hz	25% of center frequency	24	64 sec	$1 \cdot 10^{-5} \text{ V Hz}^{-1/2}$ @ 19 Hz
Waveform Analyzer B-field	spin-plane search coil	0.22–448 Hz	25% of center frequency	22	64 sec	$2 \cdot 10^{-12} \text{ T Hz}^{-1/2}$ @ 3.5 Hz

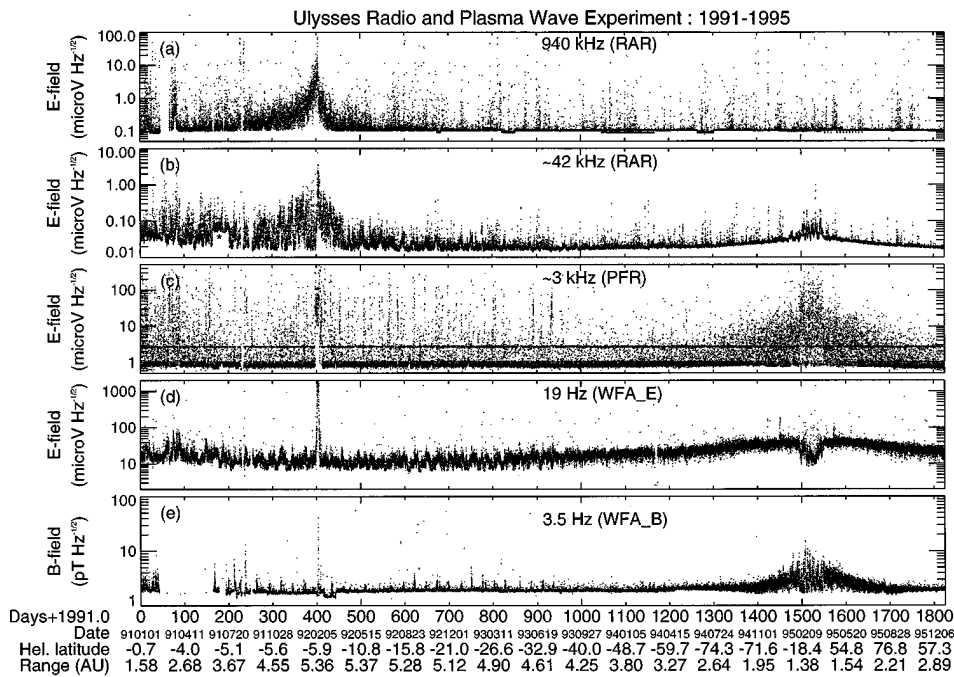


**Fig. 2a–e.** Ulysses URAP single frequency plots of wave electric or magnetic field for 5 data channels for the time interval 1991–1995. The time resolution is hourly averages or peak values; see text for details. Time, heliographic latitude, and distance from the Sun are indicated. The frequencies and URAP sub-instruments from which the data were derived are indicated for each panel. The many wave events observed are summarized in the text.

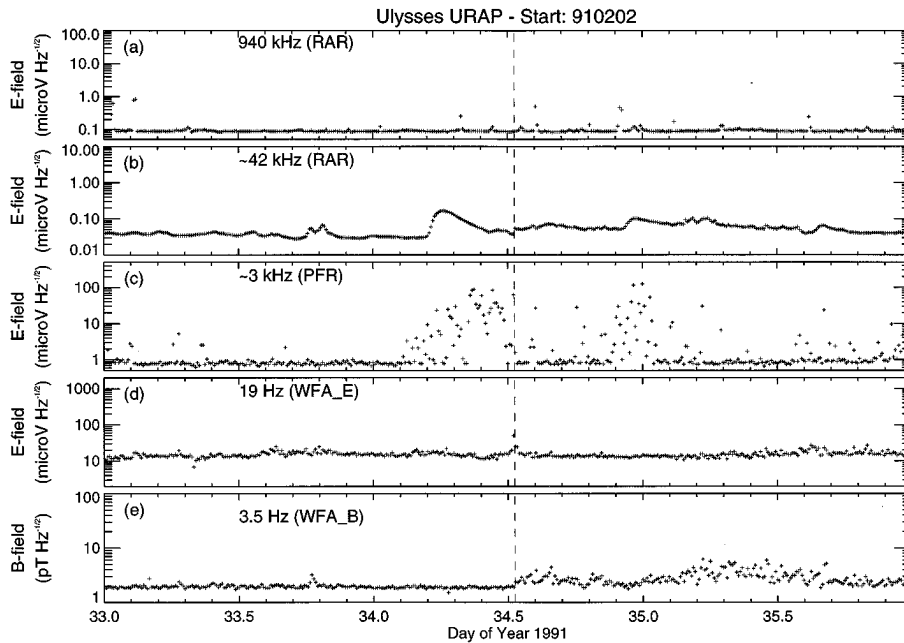
high and low-band URAP Radio Astronomy Receivers (RAR). The electric fields presented in panel (a) consist of interplanetary (IP) emissions of solar origin and Jovian magnetospheric emissions. An additional radio source at 940 kHz is the galactic background emission (Brown 1973). At 42 kHz, an additional source of electric fields is the local electron thermal noise (Meyer-Vernet and Perche 1989). In order to show the contributions of these various sources at higher time resolution, Fig. 3 presents 10 minute average data for 3 days in 1991. In Fig. 3b, the time profiles of several type III bursts are evident, whereas they appear as isolated points above the background in Fig. 2. Such radio bursts have been studied extensively in an effort to understand the complex emission and beam stabilization processes (Dulk 1990; Muschietti 1990; Melrose 1991; and references therein.) URAP observations have contributed to the clear identification of fundamental and harmonic emissions from IP type III bursts (Reiner et al. 1992), to the predominant emission mode in the leading edge of the burst (Hoang et al. 1994), to the low frequency extent of the emission (Leblanc et al. 1996), and to the understanding of the wave emission processes (Kellogg et al. 1992; Thejappa et al. 1993, and references therein).

Fig. 2a and b show a considerably higher level of emission prior to the Jupiter flyby, which occurred on February 8, 1992, than afterwards. Although some of this emission results from type III and occasionally type II solar radio bursts, a significant fraction of the emission observed prior to the flyby results from the variety of Jovian radio bursts that occur in this frequency range (Stone et al. 1992; Lecacheux et al. 1992; MacDowall et al. 1993). Major components at 940 and 42 kHz, respectively, are Jovian hectometric and broadband kilometric emissions. Shortly after the flyby, their intensities as observed from Ulysses were significantly reduced (Barrow and Lecacheux 1993), probably due to the spacecraft moving out of the primary beam of the

emissions (for the frequencies shown in Fig. 2). Consequently, a higher percentage of the bursty activity in panels (a) and (b) occurring after 1992 is type III burst emission. The number and intensity of type III bursts depends on the level of solar activity. A good indication of changes in the level of type III burst activity observed by Ulysses is given by figures in Leblanc et al. (1996), where the low frequency limits of this emission are analyzed.

The third major component observed in Fig. 2b is a (usually) smoothly varying signal level known as quasi-thermal noise, which is caused by electric field fluctuations produced by thermal electrons moving past the antenna (Maksimovic et al. 1995; Hoang et al. 1996; and references therein). At frequencies well above  $f_{pe}$ , the level of this emission depends on the electron pressure and is therefore a function of density and the distance from the Sun (Meyer-Vernet and Perche 1989). The level of quasi-thermal noise is seen to increase gradually as the spacecraft moves closer to the Sun in 1994. It undergoes abrupt variations as the spacecraft repeatedly intercepts the heliographic equator and streamer belt in 1995. In Fig. 3b a similar effect can be seen as an interplanetary shock, indicated by a dashed line, passes the spacecraft, increasing the in situ density and, therefore, the quasi-thermal noise level at frequencies above  $f_{pe}$ .

The 42 kHz data, shown in panel (b), are usually acquired with the RAR low-band receiver connected to the spin-plane dipole antenna. Occasionally, these data are the output of summation of the spin-plane dipole and spin-axis monopole antennas. In such cases, there is a significant background increase due to the shorter and thicker spin-axis antenna; the longest summed interval is indicated by an asterisk (\*) in Fig. 2b. On the other hand, the 940 kHz data in panel (a) are usually collected in summation mode. When the data correspond to the spin-plane



**Fig. 3a–e.** A 3-day plot of 10-minute resolution data in the same format as Fig. 2. The occurrence of a IP shock at approximately day 34.5 (dashed line) causes changes observed in several frequency bands, as discussed in the text.

dipole only, the effective background level is slightly lower, as seen in several intervals in Fig. 2a.

The 3 kHz data in Fig. 2c are from the URAP Plasma Frequency Receiver (PFR). The data plotted in this panel are peak values during the 1-hour (Fig. 2) or 10-min (Fig. 3) intervals; the effective time constant of the instrument is approximately 2 msec at 3 kHz. This frequency is almost always less than the in situ electron plasma frequency ( $f_{pe}$ ), and the wave activity corresponds to the time-averaged broadband waves usually known as ion-acoustic-like waves (Gurnett 1991). These waves are usually identified as Doppler-shifted ion acoustic waves (Gurnett and Frank 1978) but questions remain concerning their existence in environments where  $T_e \sim T_i$  (Gurnett 1991, Thejappa et al. 1996). The waves appear broadband when observed with low time resolution, but high time resolution observations show them to be narrow-banded tones that drift rapidly in frequency (Kurth et al. 1979). In Fig. 3c, these waves are observed to occur upstream of the interplanetary shock, as well as in downstream regions. As suggested by Fig. 2c, waves in this frequency range are common all along the Ulysses trajectory; however, they are more intense closer to the Sun. Their behavior during the fast latitude scan shows a particularly strong variation, which we examine in more detail below.

In Fig. 2d, the electric field observations at 19 Hz show signal levels which usually vary over less than an order of magnitude, unlike the electric field observations at higher frequencies. The electric fields represented here may correspond to electromagnetic or electrostatic whistler waves, lower hybrid waves, and/or long-wavelength ion-acoustic waves. The variability of the electric field on time scales less than 1 hour in this frequency range results from bursty emission with durations that are typically 10–20 min in duration. In 1991, the large scale variations are associated with shocks passing the spacecraft, producing variations similar to that seen in Fig. 3d. There, the electric field

level decreases after the passage of the forward shock. The 19 Hz electric field decreases to its lowest level in late 1992, when the spacecraft is farthest from the Sun, then gradually increases as the Sun-Ulysses distance decreases. In late 1992 through mid-1993, some of the variation on an approximately 26 day cycle is associated with the spacecraft’s repeated entry into fast solar wind that is driving a corotating interaction region. The maximum signal levels in 1995 are obtained at latitudes just outside of the streamer belt, i.e., in continuous fast wind close to the Sun. Inside the streamer belt, the emission levels show variability at levels lower than those observed in early 1991. It will be shown below that much of this change in signal level correlates with variations in solar wind density and velocity.

Fig. 2e shows the magnetic field data at 3.5 Hz, which is almost always less than the electron gyrofrequency at the spacecraft. The magnetic field variations here are likely to be due to whistler waves or electromagnetic lower hybrid waves. These data are obtained from the spin-plane search coil; spin-axis search coil data, including most of the first 300 days shown in Fig. 2, have been excluded. (Small, slowly-varying trends in the background level are due to spacecraft temperature variations.) Throughout much of the mission, the wave activity observed at this frequency only extends above the background level in regions of enhanced magnetic field amplitude, such as the downstream regions of IP shocks for which an example may be seen in Fig. 3e. In late 1992 through mid-1993, some of the activity occurring at approximately 26 day intervals is associated with the spacecraft’s repeated entry into the overdense structures comprising a corotating interaction region. It has been argued (Lengyel-Frey et al. 1994, 1996) that this occurs, at least in part, because of a general correlation between this wave activity and the magnitude of the magnetic field. Only when Ulysses approaches within about 2.5 AU of the Sun, where  $|B| > 1$  nT, does the 3.5 Hz magnetic field data rise consistently above the

instrumental background (on the time scale of 1-hour averages). During the fast latitude scan, this magnetic wave activity is also modulated during encounters with the streamer belt. It will be shown below that this variation is highly correlated with the magnitude of the magnetic field.

### 3.2. The fast latitude scan

The highly-inclined, elliptical trajectory of Ulysses has a perihelion at 1.3 AU and an aphelion at 5.4 AU. As a consequence, the perihelion pass covers  $-70^\circ$  to  $+70^\circ$  of heliographic latitude in less than 8 months. In figure 4(a-d), we present in situ wave data of 10-minute time resolution for that interval. The data from approximately  $-20^\circ$  to  $+20^\circ$  correspond to the interval when the heliospheric current sheet repeatedly intercepted the Ulysses spacecraft (Balogh et al. 1995). The intensity and variability of the wave data, as well as the solar wind and magnetic field parameters, are usually different inside and outside the streamer belt. Data from the same interval are replotted in Fig. 5 as the probability that the wave activity will exceed a given threshold. This alternate display provides a useful supplement to the scatter plots in Fig. 4. Fig. 6 is an expanded version of Fig. 4 covering the range of heliographic latitudes from  $-20^\circ$  to  $+20^\circ$  only.

It should be noted that the wave activity for panels (a) and (b) in these three figures does not correspond to constant frequencies. In order to relate the observed waves more directly to characteristic frequencies of the plasma, Ulysses plasma analyzer data are used to determine the electron plasma frequency. Panels (a) in Figs. 4-6 use the wave data obtained at the frequency closest to the electron plasma frequency; panels (b) use the frequency  $f_{pe}/3$ . In the streamer belt, the plasma frequency is usually significantly higher than at high latitudes; compare the plot of plasma density (panel (e)).

As seen in Fig. 4a, the intensities of the electric fields at  $\sim f_{pe}$  are frequently much higher outside of  $-20^\circ$  to  $+20^\circ$  than inside. This can be seen more clearly in Fig. 5a, where the probability of an electric field greater than  $5 \cdot 10^{-6} \text{ V Hz}^{-1/2}$  is shown for  $1^\circ$  bins of latitude. The probability of wave activity greater than this level occurring outside of the streamer belt is more than 3 times the probability inside the streamer belt. At approximately  $7^\circ$ , much of the intense activity is caused by Langmuir waves associated with type III burst-associated electrons that intercept the spacecraft. Waves caused by electron beams upstream of shocks may also contribute to occasional wave activity at low latitudes. The latitudes of the shocks observed at Ulysses are indicated in Figs. 4-6 by dashed lines (R. J. Forsyth, private communication). Outside of the streamer belt, almost all of the wave activity occurs in magnetic holes. These structures were discovered by Ulysses to be frequent locations of waves at  $\sim f_{pe}$  (Lin et al. 1995). As suggested by the higher probabilities of wave activity at high latitudes, magnetic holes are more common in the fast (high-latitude) solar wind, although they also occur in the ecliptic (Winterhalter et al. 1994; Balogh et al. 1995).

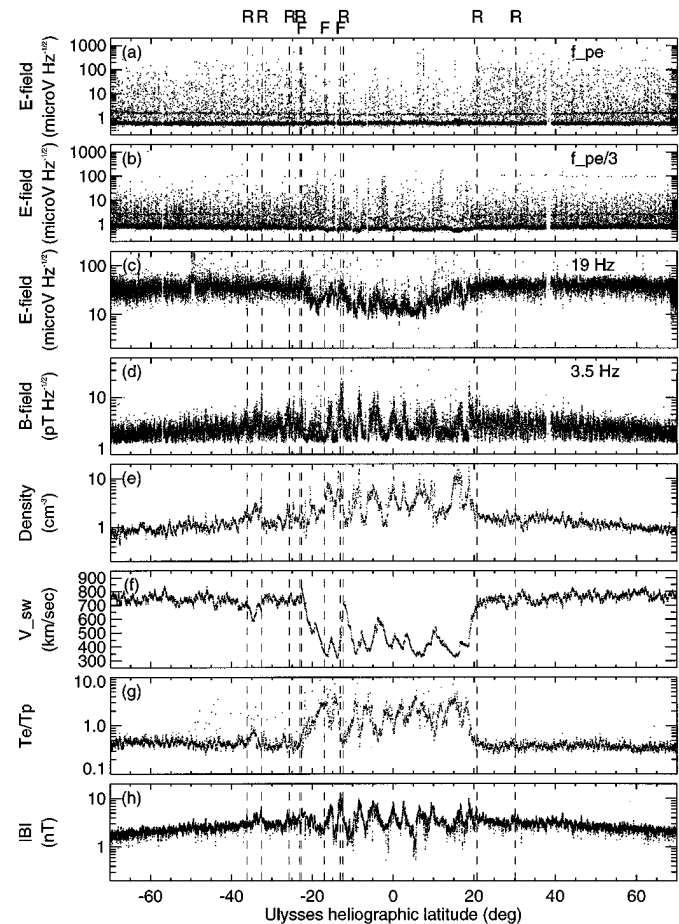


**Fig. 4a–h.** Plots of wave, plasma, and magnetic field data from the Ulysses fast latitude scan over the range of heliographic latitude from  $-70^\circ$  to  $+70^\circ$ . The wave and magnetic field panels have 10 minute time resolution, as described in the text; the plasma data have 1 hour time resolution. Note the significant differences in the wave activities at high and low latitudes. Dashed lines indicate the occurrences of forward and reverse shocks, labeled F and R, respectively.

As seen in Fig. 4b, the waves at frequencies  $\ll f_{pe}$  show a behavior very different from those at  $f_{pe}$  (presented in Fig. 4a). The most intense wave activity occurs inside the streamer belt, and the observed levels are modulated as the spacecraft flies through fast and slow speed streams. In Fig. 5b, it can be seen that the probability of wave occurrence is alternatively higher and lower in the streamer belt, compared to the occurrence probability at high latitudes. Fig. 6, which is an expanded plot of the Fig. 4 data in the streamer belt, shows that intervals of maximum activity (in panel b) are not well correlated with the variation of solar wind density (panel e) or other plasma parameters.

In Fig. 4c, the 19 Hz channel from the URAP WFA instrument shows a rapidly fluctuating level of electric field, in the restricted range from about  $2\text{--}6 \cdot 10^{-5} \text{ V Hz}^{-1/2}$ , while the spacecraft is outside of the streamer belt. From Fig. 2c, it may be seen that the signal levels increase as the spacecraft approaches the streamer belt, which is likely to be correlated with the increasing density. Inside the streamer belt, the field level at 19 Hz falls

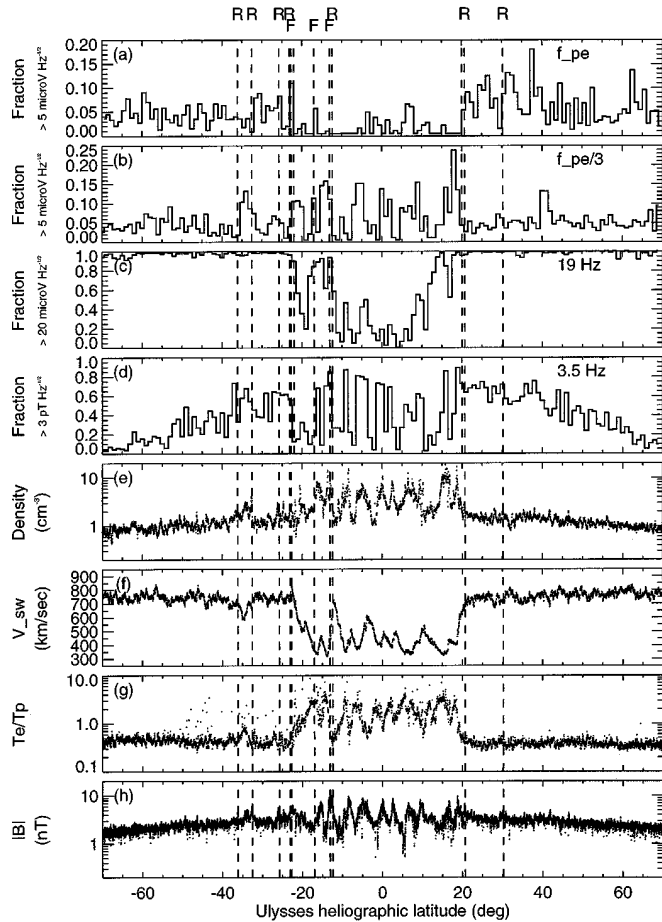


**Fig. 5a–h.** Histograms showing the probability of wave levels exceeding particular thresholds (see ordinate axis) for the wave data plotted in Fig. 4a–d. These panels (a–d) elucidate some of the significant differences in wave behavior in fast and slow solar wind. Plasma and magnetic field data are plotted in panels (e–h). Dashed lines indicate occurrences of forward and reverse shocks, as in Fig. 4.

significantly below the levels occurring outside the streamer belt. This signal level appears to vary with solar wind velocity and density. The intense event occurring at approximately  $-50^\circ$  is not correlated with unusual solar wind parameters; rather, it results from wave activity produced by firing the spacecraft thrusters. Similar, but shorter duration, intensifications are seen in Fig. 6c. The mechanism(s) responsible for the generation of this wave activity are not yet understood.

The magnetic field data shown in Fig. 4d shows a highly variable, but otherwise structureless signal outside of the streamer belt. The signal trends higher as the spacecraft approaches the streamer belt, clearly seen in Fig. 5d. Inside the streamer belt, the signal shows significant structure, extending both higher and lower than the range observed just outside the streamer belt. In Fig. 6d, it can be seen that the maximum envelope of the magnetic wave signal is well-correlated with the magnitude of the magnetic field, as discussed by Lengyel-Frey et al. (1996).

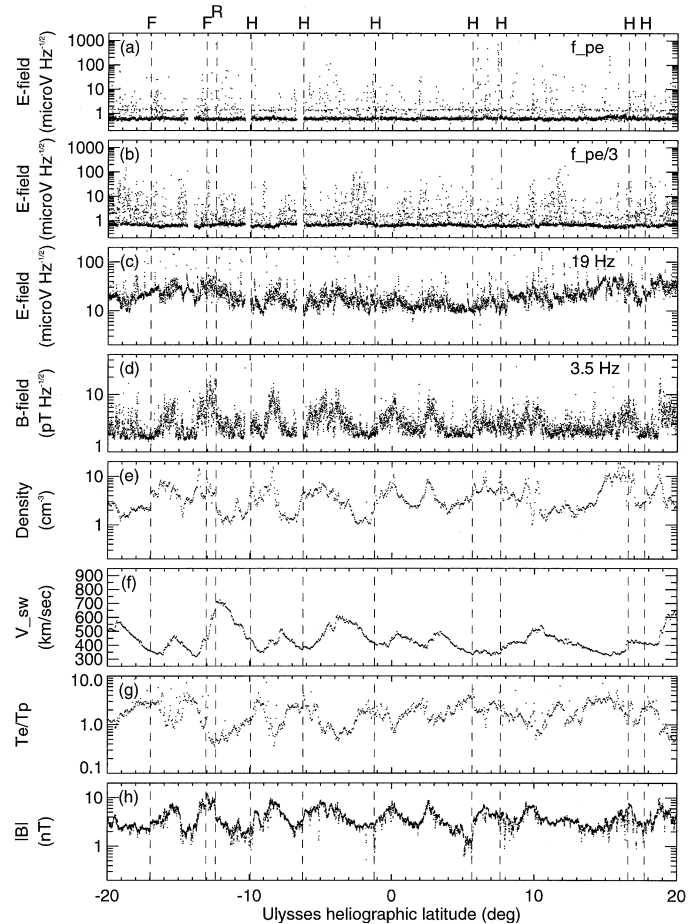


**Fig. 6a–h.** Expanded version of Fig. 4, covering the range of heliographic latitudes from  $-20^\circ$  to  $+20^\circ$ . i.e., the interval of repeated spacecraft passages through the heliospheric current sheet, which are indicated by the dashed lines labeled H.

### 3.3. Variation with distance from the Sun in fast solar wind

The variations in wave intensity with “heliographic latitude” result in large part because of the differences in solar wind parameters associated with slow, fast, and faster solar wind and in the number and kinds of discontinuities located in these different regions. Levels of wave amplitude and activity also depend on distance from the Sun, as shown in Fig. 7 for distances from 1.6 to 3.8 AU. During this time interval the spacecraft covered a latitude range of only  $31^\circ$ . Such wave variations have been explored in the ecliptic by other spacecraft, but Ulysses is the first spacecraft to measure plasma wave activity over a considerable range of distances while continuously located in fast solar wind from polar coronal holes.

In panel 7(a), bursty wave activity at  $f_{pe}$  occurs consistently over the range of distances shown. The intensity of wave bursts gradually decreases with increasing distance. It has been shown that most of these bursts are associated with magnetic holes (Lin et al. 1996); however, a definitive study of the occurrence probability of magnetic holes as a function of distance from the Sun is not yet available. The solar wind density, shown in panel 7(e),

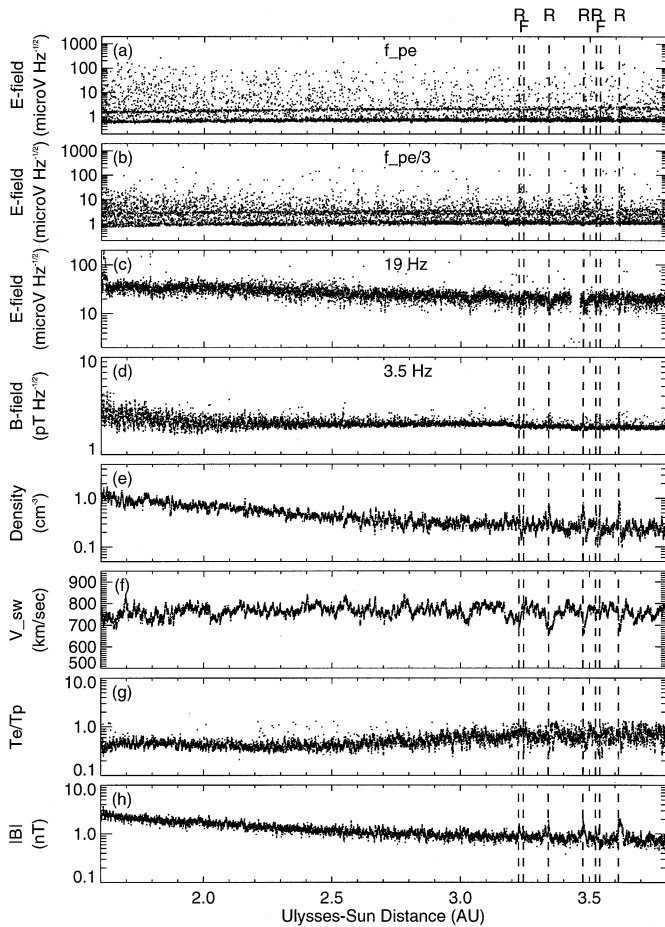


**Fig. 7a–h.** Plots of wave, plasma, and magnetic field data as a function of Ulysses–Sun distance for the inbound pass through the southern hemisphere. The format of the plot is similar to Fig. 4; however, the independent variable and data interval are different. The variations of wave activity levels, as well as those of the other parameters, are discussed in the text. Dashed lines labeled F and R indicate forward and reverse shocks, respectively.

also decreases with distance from the Sun (as approximately  $r^{-2}$ ). The lower levels of electric fields at larger distances is likely due, at least in part, to the decrease in density.

Similar trends with distance may be seen at frequencies  $\ll f_{pe}$ , shown in panel 7(b), which is the frequency range in which the wave activity is conventionally assumed to be Doppler-shifted ion acoustic waves. Note, however, that the electron-proton temperature ratio (panel 7(g)) is consistently less than 1.0 over the range 1.6 to  $> 3.0$  AU. Under such conditions, ion-acoustic waves should be strongly damped, suggesting that these waves result from another mode. Note also the occurrences of several enhanced wave events at the times of IP shocks, designated by dashed vertical lines.

In panel 7(c), the 19 Hz wave activity continues to show variability on the smallest time scales, with few significant events. The intensity decreases gradually as a function of distance from the Sun. Note also several reductions in wave activity at the

times that density increases and solar wind velocity (panel 7(f)) decreases in the presence of IP shocks.

Finally, in panel 7(d), the magnetic wave activity shows considerable short term time variability from 1.6 to about 2.5 AU; beyond that distance, the signal level is near the instrument threshold much of the time. Small variations in the background level are caused by variation in the spacecraft/detector temperatures, which have not been removed from these data.

#### 4. Discussion

The synoptic plots of remote radio emission (Fig. 2a–b) indicate relatively low levels of IP radio burst activity during solar minimum. The limited number of bursts has practical advantages; it greatly simplifies burst identification for multipoint observations and identification of the characteristics of single bursts (Barrow et al. 1996; Dulk et al. 1996; Leblanc et al. 1996). At solar maximum, the low frequency extent of type III bursts frequently blends into a nearly continuous radio emission. Using type III bursts from the interval when Ulysses and the Wind spacecraft were on opposite sides of the Sun, Dulk et al. (1996) demonstrated that about 30% of bursts observed by Ulysses and Wind have low frequency cutoffs occurring at the same frequencies (within 12% of each other). This strongly suggests that the frequency cutoffs for these bursts are intrinsic to the emission process. For other events, propagation effects and beaming may play a more important role. These studies have also demonstrated that a lower limit for type III radio emission is approximately 10 kHz. Apparently, by the time the type III emitters reach the distances from the Sun of  $\sim 2$  AU, the beam emission mechanism is no longer effective.

For in situ waves, variations along the Ulysses trajectory are much more pronounced; particularly abrupt variations occur during the fast latitude scan. For example, the levels of Langmuir waves (Figs. 4–6, panel (a)) are significantly higher outside of the streamer belt than inside. Although Langmuir waves are sometimes caused by the electrons associated with type III bursts or with shocks, the Langmuir wave activity at high heliographic latitudes is almost exclusively associated with magnetic holes or other magnetic field discontinuities (Lin et al. 1996). In the fast latitude scan data, e.g., Fig. 4a, there are only two electron streams producing type III bursts that are unambiguously associated with Langmuir waves. Shocks are also limited in number during this interval.

A high time resolution example of Langmuir waves in magnetic holes is shown in Fig. 8; other examples may be found in Lin et al. (1995, 1996). As seen in Fig. 8, the fractional decrease in the magnetic field intensity need not be larger than 0.25 to produce significant levels of Langmuir waves. Magnetic holes were first discussed in the literature by Turner et al. (1977), but their association with Langmuir wave activity was discovered by the Ulysses instruments, even though numerous spacecraft equipped with plasma wave detectors have flown previously. The discovery of Langmuir waves in magnetic holes is partly due to the URAP investigation’s high frequency resolution and also to the greater occurrence probability of these bursts (in

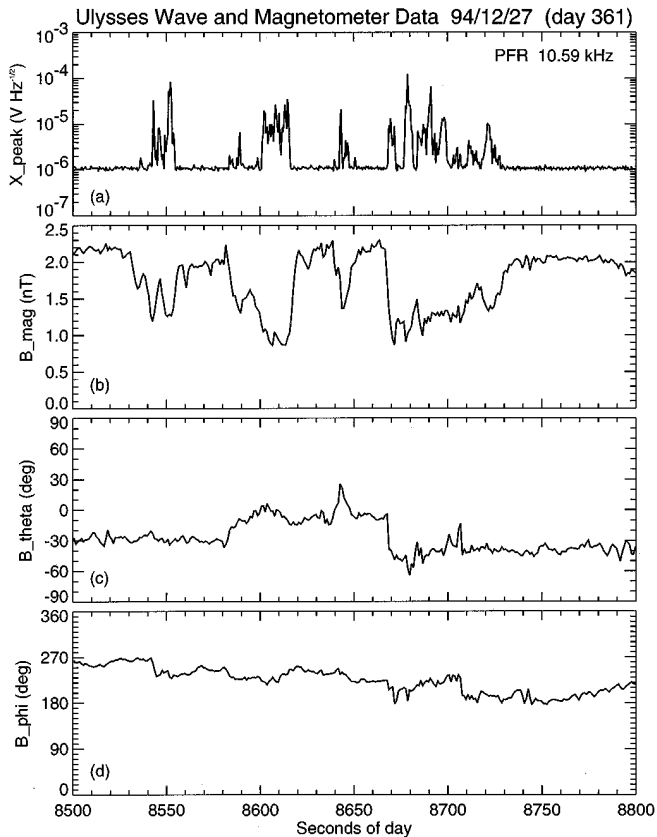


**Fig. 8.** **a** High time resolution data from the URAP PFR instrument showing a series of wave bursts occurring at the same time as magnetic holes observed by the Ulysses magnetometer, from which **b** magnetic field amplitude, **c** elevation angle, and **d** azimuth are plotted. The PFR data are peak values of electric field, measured with 0.5 sec time resolution.

magnetic holes) at high heliographic latitudes. Nevertheless, it is likely that similar bursts have been detected by all preceding missions equipped with plasma wave receivers.

The detailed explanation of the generation of Langmuir waves inside magnetic holes is not yet available, although it seems certain that it depends on unusual characteristics of the electron distribution function in magnetic holes. It has been noted by MacDowall et al. (1996) that conservation of magnetic moment could produce “anti-loss cone” electron distributions inside magnetic holes. Southwood and Kivelson (1993) have discussed similar consequences for ions in magnetic holes. On the other hand, Meyer-Vernet and Hoang (1996) have suggested that the resulting “anti-loss cone” distribution would generate low frequency waves, which might be Doppler shifted into the frequency range near  $f_{pe}$ . Furthermore, magnetic holes are also associated with electrostatic and electromagnetic waves at lower frequencies (Lin et al. 1995).

These frequently occurring instances of bursty electrostatic and electromagnetic waves have an effect on the electrons moving along the magnetic field. Based in Fig. 7a, the occurrence probability and intensity of Langmuir waves in high speed solar wind does not exhibit a strong variation with distance from

the Sun. Assuming a typical occurrence probability of 0.05 (per 10 minute interval) for waves in magnetic holes (from Fig. 5a), then a suprathermal (strahl) electron in 800 km/sec solar wind will have intercepted more than 30 magnetic holes containing electrostatic (and electromagnetic) waves by the time it reaches 2 AU. The interactions of these electrons with the localized (bursty) waves will scatter the electrons as they move outward along the magnetic field. This is likely to be one of the causes of electron strahl broadening at high heliographic latitudes, which has been reported by Phillips et al. (1995).

Comparing Fig. 5b to 5a indicates that ion-acoustic-like wave occurrence is controlled by parameters significantly different from the Langmuir wave regime. In fast solar wind, there is a relatively constant level of wave activity; inside the streamer belt, the levels of activity are typically either higher or lower than the levels observed outside the streamer belt. Examination of Fig. 6 suggests that none of the solar wind parameters plotted provides a unique explanation of the ion-acoustic-like wave variability. It is expected that the temperature ratio  $T_e/T_i$  should play a key role, because ion-acoustic waves are rapidly damped unless  $T_e/T_i \gg 1$ . Indeed, it has been shown elsewhere (Gurnett et al. 1979, Hess et al. 1996) that the intensity or occurrence probability of these waves is correlated with  $T_e/T_i$ . Nevertheless, the levels of wave activity remain quite high when  $T_e/T_i \sim 1$ , strongly suggesting that they are not the ion-acoustic mode.

The 19 Hz electric field undergoes a profound change during the passage through the streamer belt. Note that outside of the streamer belt, the 19 Hz signal shows relatively small variations with only occasional events occurring above the typical signal level. Inside the streamer belt, there is a gradual decrease, modulated by passages through the current sheet. There are some similarities in the evolution of this signal level and the variation of the solar wind velocity. It is likely that these variations depend on a combination of solar wind velocity and density. Further analysis is required to understand both the long-term trends and the short term variability of this wave activity.

The search coil data (3.5 Hz) in Fig. 4-7, panels (d), on the other hand, shows a high level of correlation with the magnetic field magnitude, as reported previously by Lengyel-Frey et al. (1994, 1996). Note the nearly complete lack of correlation between data in panels (c) and (d) in Figs. 4-7. As Ulysses passes through the streamer belt, the large variations in density and the associated changes in “frozen in” magnetic field result in variations of 3 Hz magnetic field that is alternately higher and lower than that observed outside the streamer belt. In Fig. 7, at distances beyond 2.5 AU, the signal level is usually near the instrument threshold. Gary et al. (1994) and Scime et al. (1994) have suggested that the whistler heat-flux instability is the likely source of heat flux regulation in the solar wind. The variations in whistler wave levels observed during the fast latitude scan deserve examination from that perspective. However, it is also noted (Scime et al. 1994) that the heat flux  $q$  is proportional to  $B$ . Consequently, it is difficult to identify the causal relationships between  $B$ ,  $q$ , and the whistler wave levels.

The 6-year orbit of Ulysses around the Sun will bring the spacecraft over the solar poles in 2000–2001 at approximately the maximum in the solar cycle. At this time, the wave environment observed by URAP should be substantially different from that reported in this paper. Type II and type III radio emissions from solar-related activity will occur with significantly greater frequency and intensity. Waves associated with IP shocks and coronal mass ejections will also be more common. It will be particularly interesting to observe the impact of enhanced solar activity on waves in the high-latitude solar wind.

*Acknowledgements.* We are grateful to the Ulysses project, mission operations, and data management offices for providing a nearly continuous stream of data, which greatly enhances the utility of long-duration datasets such as those presented here. We acknowledge the invaluable assistance of R. J. Forsyth in providing magnetic field data and shock identifications. RJM thanks P. J. Kellogg and K. A. Goetz for helpful discussions regarding URAP instrument characteristics. The URAP investigation is a collaboration of NASA/Goddard Space Flight Center, the Observatoire de Paris-Meudon, the University of Minnesota, and the Centre des Etudes Terrestres et Planétaires, Velizy, France.

## References

- Balogh A., Beek T.J., Forsyth R.J., et al., 1992, *A&AS*, 92, 221  
 Balogh A., Smith E.J., Tsurutani B.J., et al., 1995, *Sci*, 268, 1007  
 Bame S.J., McComas D.J., Barraclough B.L., et al., 1992, *A&AS*, 92, 237  
 Barrow C.H., Lecacheux A., 1993, *A&A*, 271, 335  
 Barrow C.H., Hoang S., MacDowall R.J., Lecacheux A., 1996, *A&A*, this issue  
 Bohm D., Gross E.P., 1949, *Phys. Rev.*, 75, 1851  
 Brown L.W., 1973, *ApJ*, 180, 359  
 Coroniti F.V., Kennel C.F., Scarf F.L., Smith E.J., 1982, *JGR*, 87, 6029  
 Dulk G.A., 1990, *Solar Phys.*, 130, 139  
 Dulk G.A., Leblanc Y., Bougeret J.-L., Hoang S., 1996, *GRL*, 23, 1203  
 Filbert P.C., Kellogg P.J., 1979, *JGR*, 84, 1369  
 Gary S.P., 1993, *Theory of Space Plasma Microinstabilities*, University Press, Cambridge, England  
 Gary S.P., Scime E.E., Phillips J.L., Feldman W.C., 1994, *JGR*, 99, 23391  
 Gurnett D.A., 1991, *Waves and Instabilities*. In: Schwenn R., Marsch, E. (eds.), *Physics of the Inner Heliosphere*, Springer-Verlag, Berlin  
 Gurnett D.A., Frank L.A., 1978, *JGR*, 83, 58  
 Gurnett D.A., Marsh, E., Pilipp W., Schwenn R., Rosenbauer H., 1979, *JGR*, 84, 2029  
 Hess R.A., Lengyel-Frey D., MacDowall R.J., Goldstein B.J., 1996, *JGR*, submitted  
 Hoang S., Dulk G.A., Leblanc Y., 1994, *A&A*, 289, 957  
 Hoang S., Meyer-Vernet N., Issautier K., Maksimovic M., Moncuquet M., 1996, *A&A*, this issue  
 Kellogg P.J., Goetz K., Howard R.L., Monson S.J., 1992, *GRL*, 19, 1303  
 Kurth W.S., Gurnett D.A., Scarf F.L., 1979, *JGR*, 84, 3413  
 Leblanc Y., Dulk G.A., Hoang S., Bougeret J.-L., Robinson P.A., 1996, *A&A*, this issue  
 Lecacheux A., Pedersen B.-M., Zarka P., et al., 1992, *GRL*, 19, 1307  
 Lengyel-Frey D., Farrell W.M., Stone R.G., Balogh A., Forsyth R., 1994, *JGR*, 99, 13325  
 Lengyel-Frey D., Hess R.A., MacDowall R.J., et al., 1996, *JGR*, in press  
 Lin N., Kellogg P.J., MacDowall R.J., et al., 1995, *GRL*, 23, 3417  
 Lin N., Kellogg P.J., MacDowall R.J., Tsurutani B.T., Ho C., 1996, *A&A*, this issue  
 Lin R.P., Levedahl W.K., Lotko W., Gurnett D.A., Scarf F.L., 1986, *ApJ*, 308, 954  
 MacDowall R.J., Kaiser M.L., Desch M.D., et al., 1993, *Plan. Space Sci.*, 41, 1059  
 MacDowall R.J., Lin N., Kellogg P.J., et al., 1996, *Proceedings, Solar Wind 8*, in press  
 Maksimovic M., Hoang S., Meyer-Vernet N., et al., 1995, *JGR*, 100, 19881  
 Manning R., Fainberg J., 1980, *Space Sci. Instr.*, 5, 161  
 Marsch E., 1985, *JGR*, 90, 6327  
 Marsch E., Chang T., 1983, *JGR*, 88, 6869  
 Melrose D. B., 1991, *Collective plasma radiation processes*, *ARA&A*, 29, 31  
 Meyer-Vernet N., Hoang S., 1996, *GRL*, in press  
 Meyer-Vernet N., Perche C. 1989, *JGR*, 94, 2405  
 Muschietti L., 1990, *Solar Phys.*, 130, 201  
 Phillips J.L., Bame S.J., Feldman W.C., et al., 1995, *Sci*, 268, 1030  
 Reiner M.J., Stone R.G., Fainberg J., 1992, *ApJ*, 394, 340  
 Rodriguez P., 1981, *JGR*, 86, 1279  
 Scarf F.L., Fredricks R. W., Frank L. A., Neugebauer M., 1971, *JGR*, 76, 5162  
 Scime E.E., Bame S.J., Feldman W.C., Gary S.P., Phillips J.L., 1994, *JGR*, 99, 23401  
 Southwood D.J., Kivelson M.G., 1993, *JGR*, 98, 9181  
 Stone R.G., Bougeret J.-L., Caldwell J., et al., 1992, *A&AS*, 92, 291  
 Stone R.G., MacDowall R.J., Fainberg J., et al., 1995, *Sci*, 268, 1026  
 Thejappa G., Lengyel-Frey D., Stone R.G., Goldstein M.L., 1993, *ApJ*, 416, 831  
 Thejappa G., Wentzel D.G., Stone R.G., 1995, *JGR*, 100, 3417  
 Thejappa G., MacDowall, R.J., Stone, R.G., et al., 1996, *JGR*, submitted  
 Thompsen M.F., Barr H.C., Gary S.P., Feldman W., Cole T.E., 1983, *JGR*, 88, 3035  
 Turner J.M., Burlaga L.F., Ness N.F., Lemaire J.F., 1977, *JGR*, 82, 1921  
 Tokar R.L., Gurnett D.A., Feldman W.C., 1984, *JGR*, 89, 105  
 Vaisberg O.L., Galeev A.A., Zastenker G.N., et al., 1983, *Soviet Phys. JETP*, 58, 716  
 Winterhalter D., Neugebauer M., Goldstein B.E., et al., 1994, *JGR*, 99, 23,371